Metal-Free B, N co-Doped Hierarchical Porous Carbon Electrocatalyst with an Excellent O₂ Reduction Performance

Fangxiao Wang[+], Jianhai Ren[+], Zihao Zheng, Qiye Liu, and Chun-yang Zhang*[a]

Fuel cells have attracted increasing attention due to their low cost, high energy density, low environmental pollution, and abundant raw materials. Oxygen reduction reaction (ORR) is a core technology of fuel cells, and the development of new electrocatalysts with high ORR performance is highly desirable. Herein, we synthesize a series of B, N co-doped hierarchical porous carbons using a soft template method with the integration of self-assembly, calcination and etching. The obtained materials exhibit hierarchical porous structures, controllable pore distribution, partial graphite structures, and B, N co-doping. They can function as the cost-effective and metal-free electrocatalysts, facilitating the diffusion of electrolyte ions and the improvement of ORR performance. Especially, the B, N co-doped porous carbon with the B-to-N molar ratio of 5 (BNC-5) displays a high ORR activity with a half-wave potential ($E_{1/2}$) of 0.73 V, an onset potential (E_{onset}) of 0.94 V, and a high limiting current density (J_L) of 5.98 mA cm^{-2}, superior to the N-doped C (NC) and BNC-1 (the B-to-N molar ratio = 1), BNC-3 (the B-to-N molar ratio = 3) and BNC-7 (the B-to-N molar ratio = 7) under the identical conditions. Moreover, the BNC-5 exhibits good cycling stability after 5000 cyclic voltammetry (CV) cycles and excellent tolerance toward even 3 M methanol. This research provides a new approach for the facile synthesis of dual element-doped carbon electrocatalysts with high ORR performance.

1. Introduction

The excessive dependence upon fossil fuel energy causes serious environmental crisis, and the development of renewable and sustainable energy is urgent.[1] Fuel cells have attracted increasing attention due to their low cost, high energy density, low environmental pollution, and abundant raw materials.[2] Oxygen reduction reaction (ORR) is a core technology of fuel cells, and the development of new electrocatalysts with high ORR performance is highly desirable.[3] In general, platinum and transition-metal materials possess large amounts of metal sites which can induce uneven charge distribution and the improvement of O₂ adsorption and reduction, and they have functioned the excellent electrocatalysts for ORR.[4–6] Nevertheless, the high cost, relatively limited stability, scarce resources, and the unsatisfactory methanol tolerance hinder their commercial

applications.[7–8] Therefore, the development of cost-effective ORR electrocatalysts with high activity has remain a challenge.

Metal-free heteroatom-doped carbon composites may function as the promising electrocatalysts to replace platinum and transition-metal materials for ORR due to their distinct advantages of high activity, low cost, and superior durability.[9–11] The doping of N onto the carbon composites is an efficient method to boost ORR catalytic activity, because more electronegative N can induce charge delocalization around the carbon network and the imminent C can turn into active reaction sites for adsorption and oxygen reduction.[12–15] Despite a few exceptions,[10] the N-monodoped carbons usually possess higher performance than most of nonmetal element-monodoped carbons prepared by the similar routes. The N-doping of pyridinic-N, pyrrolic-N, and graphitic-N are extensively applied for the construction of metal-free carbon-based electrocatalysts.[16] Besides the single-atom doping, the heteroatom co-doping can facilitate the enhancement of electrochemical performance of carbon materials.[17] Simultaneous incorporation of one electron-rich atom (e.g., N) and one electron-deficient atom (e.g., Al or B) can generate a special electronic system with synergistic effect, resulting in the enhanced electrochemical performance.[18] The insertion of electron-deficient atom B into the carbon materials can function as the ORR active site due to the generation of B$^+$ site for O₂ and ORR.[19–21] In addition, the introduction of boron and nitrogen into a sp² C—C π-conjugated system network may slightly affect the atomic arrangement, because N, B and C have similar atomic radius which can prevent the lattice mismatch.[22] Consequently, the co-doping of metal-free heteroatoms may offer an efficient strategy for the fabrication of high-performance porous carbon electrocatalysts.

[a] F. Wang,[+] J. Ren,[+] Z. Zheng, Q. Liu, Dr. C.-y. Zhang
College of Chemistry, Chemical Engineering and Materials Science
Collaborative Innovation Center of Functionalized Probes for Chemical
Imaging in Universities of Shandong
Key Laboratory of Molecular and Nano Probes
Ministry of Education
Shandong Provincial Key Laboratory of Clean Production of Fine Chemicals
Shandong Normal University
Jinan 250014 (China)
E-mail: cyzhang@sdnu.edu.cn

[+] These authors contributed equally to this work.

Supporting information for this article is available on the WWW under
https://doi.org/10.1002/open.202100090

ChemistryOpen

Full Papers
doi.org/10.1002/open.202100090

Chemistry Europe
European Chemical
Societies Publishing

Herein, we prepare a series of B, N co-doped porous carbons (BNCs) using a soft template method. This method integrates the facile self-assembly process with the carbonization and etching to produce large amounts of BNCs with the characteristics of hierarchical porous structures (micro – meso – macro-porous), controllable pore distribution, partial graphite structures, and B, N co-doping, which greatly facilitates the diffusion of electrolyte ions and the improvement of ORR performance. The obtained B, N co-doped porous carbon with the B-to-N molar ratio of 5 (BNC-5) can function as the efficient and cost-effective metal-free electro-catalyst, with a higher ORR activity (E_{onset}: 0.94 V vs. RHE, $E_{1/2}$: 0.73 V vs. RHE, J_L: 5.98 mA cm^{-2}) than the N-doped C (NC), BNC-1 (the B-to-N molar ratio = 1), BNC-3 (the B-to-N molar ratio = 3) and BNC-7 (the B-to-N molar ratio = 7) under the identical conditions. Moreover, the BNC-5 possesses good cycling stability after 5000 CVs cycles and excellent tolerance toward even 3 M methanol.
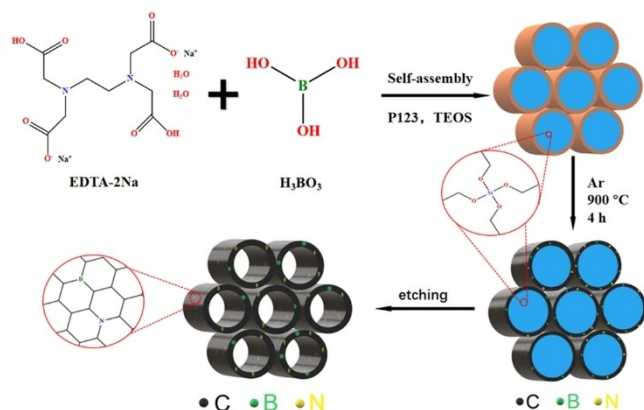
Scheme 1. Schematic illustration for the synthesis of the B/N co-doped porous carbon materials.
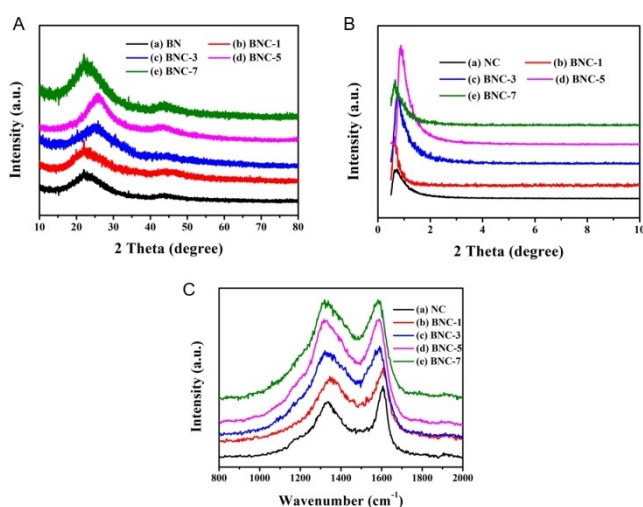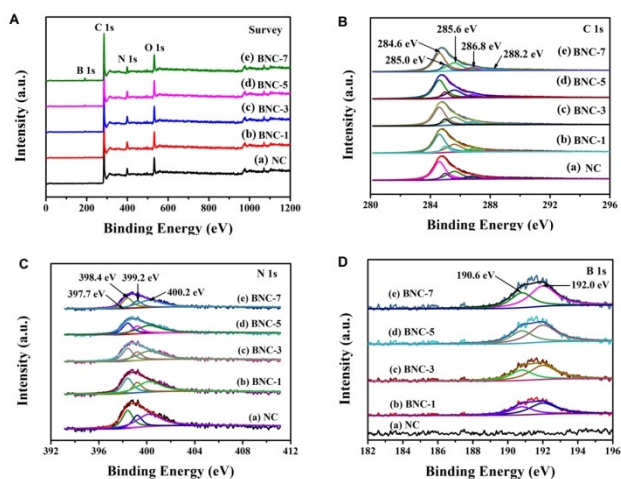

Figure 1. (A–C) Wide (A), small (B) angle XRD patterns and Raman spectra (C) of NC (a, black color), BNC-1 (b, red color), BNC-3 (c, blue color), BNC-5 (d, pink color), and BNC-7 (e, green color).

2. Results and Discussion

Scheme 1 illustrates the synthesis of the B, N co-doped porous carbon materials by utilizing a soft template method. Briefly, the EDTA-2Na and H_3BO_3 are dissolved in distilled water containing P123 soft template, and then TEOS is added to obtain a gelatinous white gel through the self-assembly process. Subsequently, the dried gel is calcinated at high temperature of 900 °C in Ar atmosphere in a tubular furnace for 4 h. After naturally cooling to 20 °C, the calcined sample is etched using 2 mol L^{-1} NaOH to produce the B, N co-doped porous carbon materials with mesoporous structures.

The crystal structure of the B, N co-doped porous carbon is characterized through wide and small angle XRD. In wide angle XRD patterns (Figure 1A), all obtained composites exhibit two clear diffraction peaks at 24° and 44°, respectively, corresponding to the (0 0 2) and (1 0 0) diffraction of carbon,[23] but no diffraction peak associated with other species is observed. When NC is turned into BNC-5, the slight shift of the (0 0 2) diffraction peak to the higher angle reveals the increase of carbon graphitization induced by the increased boric acid.[24,25] In small angle XRD patterns (Figure 1B), the NC, BNC-1 (the B-to-N molar ratio = 1), BNC-3 (the B-to-N molar ratio = 3), BNC-5 (the B-to-N molar ratio = 5) and BNC-7 (the B-to-N molar ratio = 7) composites exhibit significant diffraction peaks at around $2\theta = 1.0°$, corresponding to (1 0 0) plane of carbon. When NC is turned into BNC-5, the shift of (1 0 0) diffraction peak to the higher angle further confirms that the B-doping can boost the graphitization of carbon. However, the shift of diffraction peaks of BNC-7 at $2\theta = 1.0°$ (Figure 1B) and $2\theta = 24$ (Figure 1A) to the lower angles might result from the collapse of pore structure induced by the excessive boric acid during high temperature-calcination.[26] To obtain more information of carbon structures, we measured the Raman spectra (Figure 1C). The introduction of heteroatoms induces slight increase in the ratio (I_D/I_G) of D band (1330 cm^{-1}) to G band (1590 cm^{-1}), suggesting the generation of a higher degree of graphite during the doping and pyrolysis procedures.[27]

We further investigated XPS spectra of the NC and B, N co-doped porous carbons. In the survey spectra (Figure 2A), the signals of C, N, B, O elements are detected in the B, N co-doped porous carbon, but no B element is detected in the NC. The high-resolution C 1s spectrum (Figure 2B) can be fitted into 284.6 (C–C), 285.0 (C 1s), 285.6 (C–N), 286.8 (C–O) and 288.2 eV (C–B) by using XPS Peak software, indicating the successful co-doping of N and B into the carbon materials.[28] The N 1s spectra (Figure 2C) can be deconvoluted into four peaks at 397.7 eV (N–B (N-1)), 398.4 eV (pyridinic-N (N-2)), 399.2 eV (graphitic-N (N-3)) and 400.2 eV (pyrrolic-N (N-4)), further confirming the successful doping of N into the carbon materials. The N-2 and N-4 doping can facilitate the stabilization of carbon structure and the enhancement of electrocatalytic performance,[29] and N-3 doping may improve the conductivity of porous carbon by offering electrons, increasing the charge density in the C–C sp^2 π-conjugated system, and boosting the four-electron ORR performance.[30] The B 1s signal (Figure 2D) can be divided into two peaks at 190.6 eV and 192.0 eV, which corresponds to B–N

ChemistryOpen

Full Papers
doi.org/10.1002/open.202100090

Chemistry Europe
European Chemical
Societies Publishing

Figure 2. The XPS patterns of (A) survey, (B) C 1s, (C) N 1s and (D) B 1s of BNC-5.

and BCO_2 groups, respectively, further confirming that the doping of B into the B, N co-doped porous carbon can induce the polarization of carbon.[31,32] Table 1 shows the XPS results of different composites. Oxygen and carbon contents (atomic %) remain unchanged in all samples. The order of boron contents in the various BNC samples is BNC-7 > BNC-5 > BNC-3 > BNC-1 > NC, consistent with the amounts of boric acid added. The order of nitrogen contents in the various BNC samples exhibits an opposite trend. When N and B are doped in BNC-5, nitrogen-doping can induce improved electrical conductivity and enhanced electrocatalytic activity, and boron can induce the carbon atom polarization and its synergetic effect with nitrogen atom can improve the ORR performance.
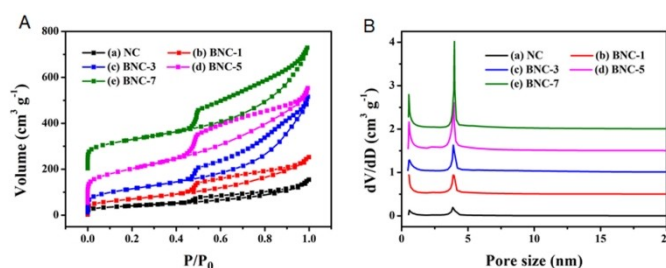
Nitrogen adsorption/desorption isotherms were conducted to analyze the pore structure characteristics (e.g., specific

Table 2. Pore structured parameters and the ORR voltametric characteristics of the obtained composites.

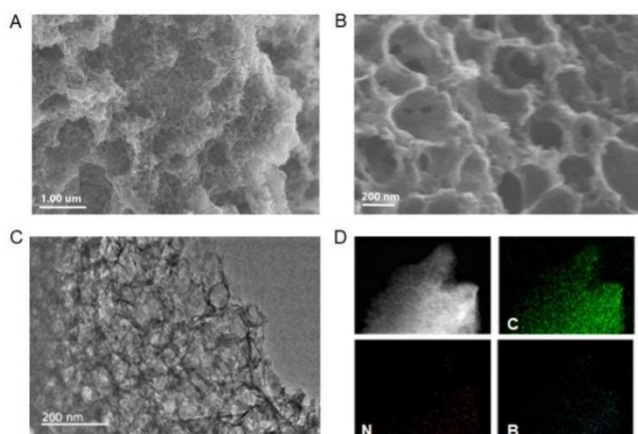| samples	BET [m^{2}g^{-1}]	V [cm^{3}g^{-1}]	D [nm]	E$_{onset}$ [V]	J$_L$ [mA cm^{-2}]
NC	144.3	0.058	0.58,3.86	0.82	2.25
BNC-1	251.7	0.159	0.51,3.91	0.85	3.65
BNC-3	404.2	0.112	0.61,3.87	0.88	4.16
BNC-5	542.6	0.847	0.51,3.88	0.94	5.98
BNC-7	457.5	0.899	0.54,3.98	0.91	5.78

surface area, pore volume and pore size distribution) of the obtained composites. The surface area and microporosity/mesoporosity have significant effect upon the electron migration, the reaction site exposure, the O_2 adsorption and reduction in ORR process.[33–36] The N_2 adsorption isotherms of the obtained composites exhibit typical I–IV hybrid isotherms at −196 °C according to the IUPAC classification (Figure 3), suggesting that they are typical micro-mesoporous materials.[37] In comparison with NC (144.3 m^{2}g^{-1}), the BET surface areas are improved to 251.7 m^{2}g^{-1} for BNC-1, 404.2 m^{2}g^{-1} for BNC-3, 542.6 m^{2}g^{-1} for BNC-5, and 457.5 m^{2}g^{-1} for BNC-7, respectively, due to the addition of boric acid. The boric acid may function as a pore expander agent, and it can be decomposed to form the C−B bond in the B, N co-doped carbon materials after high temperature-calcination in Ar atmosphere.[27] Notably, the decrease of specific surface in BNC-7 may result from the collapse of pores induced by the excessive amount of boric acid, consistent with the XRD results (Figure 1). Table 2 shows the pore structure characteristics of the obtained NC and BNC composites. Among them, BNC-5 possesses the largest pore volume (0.847 cm^{3}g^{-1}) and the largest specific surface area (542.6 m^{2}g^{-1}) which can provide more catalytic active centers. In addition, the pores of BNC-5 can provide ample regions for the charges transfer during catalytic reaction, greatly improving the ORR efficiency.

The SEM (Figures 4A–B) and TEM (Figure 4C) show the macroscopic appearance and microscopic pore structure of BNC-5. BNC-5 possesses an ordered array with a hierarchical porous structure (Figure 4A), confirming the presence of the micropores with a dominant pore size of 0.51 nm, the mesopores with a distribution pore size of 3.88 nm, and the macropore with an average pore size of 100 nm. The hierarchical porous structure of BNC-5 not only facilitates the transport

Table 1. XPS results of different composites.

samples	C [at%]	O [at%]	B [at%]	N [at%]
NC	76.04	12.19	0	11.77
BNC-1	75.76	11.84	1.37	11.03
BNC-3	75.52	11.68	2.61	10.19
BNC-5	75.47	11.79	4.98	7.76
BNC-7	75.63	11.49	7.24	5.64

Figure 3. (A) N_2 adsorption-desorption thermal curve and (B) pore size distribution of NC (a, black), BNC-1 (b, red), BNC-3 (c, blue), BNC-5 (d, pink) and BNC-7 (e, green) composites.

ChemistryOpen

Full Papers
doi.org/10.1002/open.202100090

Chemistry Europe
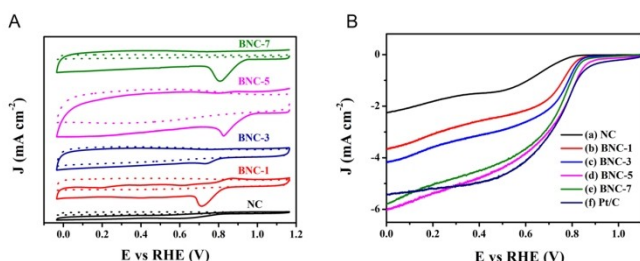European Chemical
Societies Publishing

Figure 4. (A, B) SEM images, (C) TEM image and (D) the corresponding elemental mapping patterns of BNC-5 composite.

of O_2 and electrolyte, but also provides more three-phase reaction space for ORR. The TEM image of BNC-5 (Figure 4C) exhibits a macropore size of 100 nm. The TEM-EDX elemental mapping analysis (Figure 4D) verifies the uniformly distribution of N, B and C on the surface of BNC-5, which facilitates the enhancement of ORR activity.

We investigated the ORR activity of NC and BNC composites in alkali media, respectively (Figure 5A). The CV curves of the obtained composites display well-defined cathodic peaks in 0.1 M KOH electrolyte containing saturated O_2, but disappear under the N_2-saturated electrolyte. The BNC-1 composite exhibits a more positive potential of cathodic peak at 0.72 V vs RHE than the NC composite (0.66 V), suggesting that the doping of boron in BNC-1 creates new reaction sites to boost the performance of ORR. With the increasing content of boron, the potential of cathodic peak further shifts to 0.76 V for BNC-3, 0.84 V for BNC-5, and 0.82 V for BNC-7, respectively. Among them, the BNC-5 exhibits the most positive cathodic peak (0.84 V vs RHE) due to the appropriate B-to-N molar ratio and the highest surface area (542.6 $m^2 g^{-1}$). However, despite the abundant B content in BNC-7, its cathodic peak at 0.82 V (vs RHE) decreases slightly due to its low surface area (457.5 $m^2 g^{-1}$) and the lack of effective reaction sites. The linear sweep

voltammetries (LSV) on the electrode of rotating disk (RDE) are further used to compare the catalytic activities of NC and BNC composites (Figure 5B). The measured limiting current density (J_L) is 2.25 $mA cm^{-2}$ for NC, 3.65 $mA cm^{-2}$ for BNC-1, 4.16 $mA cm^{-2}$ for BNC-3, 5.98 $mA cm^{-2}$ for BNC-5, and 5.78 $mA cm^{-2}$ for BNC-7, respectively. The onset potential (E_{onset}) is 0.82 V (vs RHE) for NC, 0.85 V for BNC-1, 0.88 V for BNC-3, 0.94 V for BNC-5, and 0.91 V for BNC-7, respectively, indicating that the order of ORR activity is NC < BNC-1 < BNC-3 < BNC-7 < BNC-5. In addition, the order of half-wave potentials ($E_{1/2}$) is NC (0.59 V) < BNC-1 (0.68 V) < BNC-3 (0.70 V) < BNC-7 (0.71 V) < BNC-5 (0.73 V) vs RHE. Moreover, the diffusion-limited current density of BNC-5 (5.98 $mA cm^{-2}$) is higher than that of commercial Pt/C (5.43 $mA cm^{-2}$). Table 3 shows the ORR parameters of NC and BNC composites. The BNC-5 exhibits the best ORR performance with the most positive E_{onset} (0.94 V) and the highest reduction current density (5.98 $mA cm^{-2}$), superior to the metal-free catalysts BN-CA-900 (E_{onset} of 0.91 V, J_L of 5.7 $mA cm^{-2}$),[3] NB—CN (E_{onset} of 0.92 V, J_L of < 5 $mA cm^{-2}$),[9] N—C composite (E_{onset} of 0.89 V, JL of < 4 $mA cm^{-2}$),[38] and the metal-containing catalysts Co/CNT/MCP-850 (E_{onset} of 0.94 V, J_L of 4.8 $mA cm^{-2}$),[6] Mn-N-C-950-AT (E_{onset} of 0.92 V, J_L of ~4 $mA cm^{-2}$),[39] and comparable to Pt/C (E_{onset} of 0.95 V, J_L of 5 $mA cm^{-2}$).[40]

We further investigated the ORR kinetics by analyzing the electron transfer number (n) according to the Koutecky-Levich (K—L) equation.[18] The current density of the NC, BNC-1, BNC-3, BNC-5 and BNC-7 electrodes enhances with the increasing rotation speed, respectively (Figures. 6 A and S1) due to the shorten diffusion distance under the high speeds. The linearity of K—L plots (Figure 6B) suggests the first-order reaction kinetics for the oxygen reduction process. The calculated number of electron transfer is 4 for BNC-5 at potentials in the range from 0.1 to 0.5 V vs RHE (Figure 6B), suggesting the 4-electron ($4e^-$) reaction path for the ORR on the BNC-5 electrode. The calculated number of electron transfer is 2 for NC, 2 and 4 for BNC-1, 4 for BNC-3, and 4 for BNC-7, respectively, suggesting that the reaction pathway undergoes $2e^-$ process for NC, $2e^-$ and $4e^-$ processes for BNC-1, and $4e^-$ process for BNC-3 and BNC-7 (see supporting information, Figure S2). These results demonstrate that the doped B can induce both the synergetic effect with N and a $4e^-$ reaction pathway to achieve high ORR performance. In general, O_2 reduction can be carried out by either indirect or direct four-electron process. The indirect four-
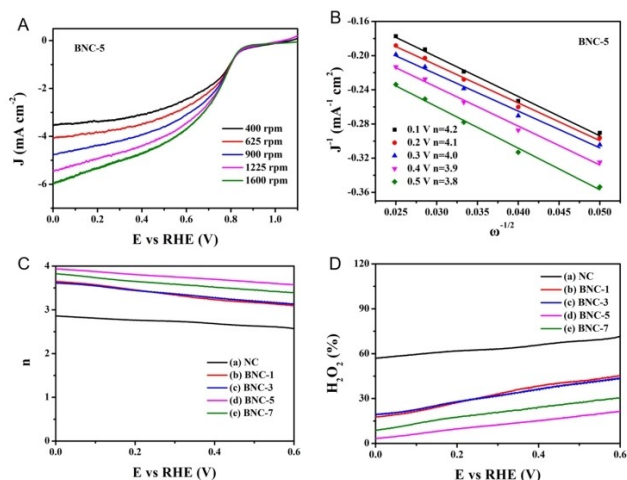

Figure 5. (A and B) CV curves (A) of NC (a, black color), BNC-1 (b, red color), BNC-3 (c, blue color), BNC-5 (d, pink color), BNC-7 (e, green color), and Pt/C (f, navy blue) composites in the N_2-saturated (dotted lines) and the O_2-saturated (solid lines) electrolytes and their LSV curves (B) at a rotation speed of 1600 rpm and a sweep rate of 10 $mV s^{-1}$.

Table 3. Comparison of the ORR performance of different composites.

electrocatalyst	E_{onset} [V vs. RHE]	$E_{1/2}$ [V vs. RHE]	J_L at 1600 rpm [$mA cm^{-2}$]	Ref.
BN-CA-900	0.91	0.77	5.7	[3]
Co/CNT/MCP-850	0.94	0.8	4.8	[6]
NB—CN	0.92	0.835	< 5.0	[9]
N—C sample	0.89	0.75	< 4.0	[38]
Mn-N-C-950-AT	0.92	0.81	~4	[39]
Pt/C	0.95	0.83	5.0	[40]
BNC-5	0.94	0.73	5.98	This work

ChemistryOpen

Full Papers
doi.org/10.1002/open.202100090

**Chemistry
Europe**
European Chemical
Societies Publishing

Figure 6. (A and B) LSV (A) of BNC-5 composite at different rotation rate and the K–L plots (B) calculated from the corresponding LSV curves. (C and D) Electron transfer number n (C) and H_2O_2 yield (D) of NC (a, black color), BNC-1 (b, red color), BNC-3 (c, blue color), BNC-5 (d, pink color) and BNC-7 (e, green color) composites.

electron process contains two consecutive steps: (1) O_2 is first reduced by two electrons to form an intermediate peroxide (H_2O_2) ($O_2 + 2H^+ + 2e^- \rightarrow H_2O_2$), and (2) the peroxide is reduced by two electrons to generate hydroxide (OH^-) ($H_2O_2 + 2e^- \rightarrow 2OH^-$). In contrast, the direct four-electron process contains only one step with O_2 being directly reduced by four electrons to OH^- ($O_2 + 2H^+ + 4e^- \rightarrow 2OH^-$).[41] Further evidence for the reaction paths is obtained by electrochemical analysis of rotating ring-disk electrode (RRDE) (Figure 6C). In the range from 0.1 to 0.5 V vs RHE, BNC-5 yields the intermediate peroxide (H_2O_2) with less than 15%, suggesting that BNC-5 undergoes a high n value of 3.7–3.92 and a process of $4e^-$ reduction pathway. In contrast, the H_2O_2 yield is 55–66% for NC, 15–39% for BNC-1, 16–38% for BNC-3, and 8–25% for BNC-7, suggesting a lower n value of 2.68–2.9 for NC, 3.22–3.7 for BNC-1, 3.24–3.68 for BNC-3, 3.5–3.84 for BNC-7, respectively.

We further measured the electrochemical impedance spectra (EIS) and the electrochemical active surface areas (ECSA) of the obtained composites. The EIS spectra (Figure 7A) are used to study the charge transfer behavior, conductivity and the electrochemical reaction kinetics of the obtained catalysts.[42]

The equivalent circuit (Figure 7B) is obtained from the EIS tests, where R_s is the resistance of solution in the tested system, C_{dl} is the double-layer capacitance between the interface of working electrode and electrolyte, R_{ct} is the resistance of charge-transfer resulting from the residual Faradaic processes, and W is the Warburg impedance. In principle, the smaller arc means the smaller charge transfer resistance and the higher electron transfer efficiency.[43] The NC composite exhibits the largest arc and the largest charge-transfer resistance, which limits the electron transfer speed. The co-doping of B and N induces the decrease of both arc radius and charge-transfer resistance for BNC catalysts, benefiting the improvement of charge transfer. Among them, BNC-5 composite exhibits the lowest charge transfer resistance and the highest electron transport at the interface.

The electrochemical active surface area (ECSA) can be estimated based on equation 1.

$$ECSA = C_{dl}/C_s \qquad (1)$$

wherein C_s is the specific capacitance and C_{dl} is the electrochemical double-layer capacitance. For carbon-based material, C_s is uniform, and the ECSA value can be reflected by the C_{dl} value. The C_{dl} is estimated by measuring the non-Faradaic region at different scan rates of cyclic voltammograms (CVs). Figures 8A–E shows the C_{dl} curves of the obtained composites at various scan rates in 0.1 M KOH solution. The double-layer charging current (i_c) can be estimated based on equation 2.
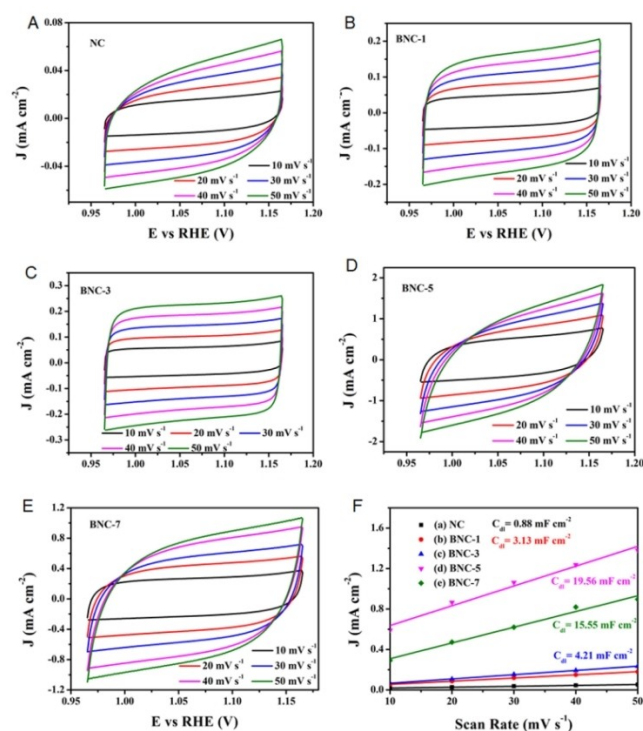

Figure 7. (A) Electrochemical impedance spectra of NC (black color), BNC-1 (red color), BNC-3 (blue color), BNC-5 (pink color), and BNC-7 (green color) composites. (B) The equivalent circuit model of electrochemical impedance tests.

Figure 8. Electrochemical double layer capacitance curves of (A) NC, (B) BNC-1, (C) BNC-3, (D) BNC-5, and (E) BNC-7 at different scan rates in the range from 50 mV s^{-1} to 10 mV s^{-1} in 0.1 M KOH. (F) The C_{dl} plots of NC (a, black color), BNC-1 (b, red color), BNC-3 (c, blue color), BNC-5 (d, pink color), and BNC-7 (e, green color).
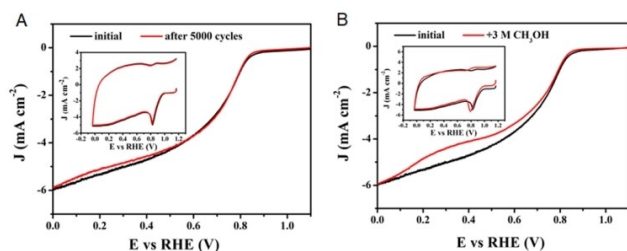
ChemistryOpen

Full Papers
doi.org/10.1002/open.202100090

Chemistry Europe
European Chemical
Societies Publishing

$$i_c = \nu C_{dl} \tag{2}$$

where ν is the scan rate. The i_c value and ν value are positively correlated, and the slope equals to C_{dl} (Figure 8F). The C_{dl} value is measured to be 0.88 mF cm^{-2} for NC, 3.13 mF cm^{-2} for BNC-1, 4.21 mF cm^{-2} for BNC-3, 19.56 mF cm^{-2} for BNC-5, and 15.55 mF cm^{-2} for BNC-7, respectively. Among them, BNC-5 exhibits the largest ECSA and the highest ORR activity.

Besides the highest ORR activity, BNC-5 possesses good durability. The E_{onset} and the half-wave potential of BNC-5 composite exhibit no significant decrease even after 5000 cycles tests in the range from −0.05 to 1.15 V (vs RHE) in oxygen-saturated 0.1 M KOH solution (Figure 9A), suggesting the good stability of BNC-5. Moreover, the BNC-5 displays excellent tolerance toward 3 M methanol, and its half-wave potential exhibits only a slightly shift of 23 mV (Figure 9B).

3. Conclusion

We have successfully synthesized the metal-free and graphitized B and N co-doped porous carbon material (i.e., BNC-5 composite) which possesses the high surface area of 542.6 m^2 g^{-1}. The BNC-5 composite can function as the cost-effective and metal-free electrocatalyst, and it exhibits high ORR activity ($E_{onset} = 0.94$ V vs. RHE, $E_{1/2} = 0.73$ V vs. RHE, $J_L = 5.98$ mA cm^{-2}), superior to the NC and other B, N dual-doped carbons (i.e., BNC-1, BNC-3 and BNC-7 composites) under the identical conditions. Moreover, the BNC-5 composite exhibits good cycling stability after 5000 cyclic voltammetries (CVs) cycles and excellent tolerance toward even 3 M methanol. The high catalytic performance of BNC-5 is ascribed to its high graphitization, high surface area, hierarchical porous structure, and the uniform N and B doping. This research provides a new avenue for the facile synthesis of dual element-doped carbon electrocatalysts with high ORR performance.

Experimental Section

Synthesis of B and N co-Doped Mesoporous Carbons

Synthesis of B and N co-doped mesoporous carbon: The 2.00 g of P123, 4.49 g of EDTA disodium salt dehydrate, and a certain amount of boric acid (the B-to-N molar ratio of 1, 3, 5 and 7, respectively) were dissolved with continuous stirring in 70 mL of ultrapure water. Then 4.6 mL of TEOS was added slowly and dropwise to the above homogeneous solution and stirred at 40 °C for 30 min. Then the obtained sol was transferred to the autoclave and treated with a hydrothermal method in an oven for 24 h at 100 °C. Subsequently, the obtained gelatinous white gel was dried in vacuum for 12 h at 100 °C. Finally, the dried gel was calcination at 900 °C in Ar atmosphere in a tubular furnace for 4 h. After naturally cooling to 20 °C, the calcined sample was etched with 2 mol L^{-1} NaOH to remove the residual silica, followed by washing and drying. The obtained products were named as BNC-1 (the B-to-N molar ratio = 1), BNC-3 (the B-to-N molar ratio = 3), BNC-5 (the B-to-N molar ratio = 5) and BNC-7 (the B-to-N molar ratio = 7), respectively. The control group without boron doping was named as the NC.

The detailed characterizations and electrochemical measurements are provided in the Supporting Information.

Conflict of Interest

The authors declare no conflict of interest.

Keywords: fuel cells · heteroatoms doping · metal-free systems · oxygen reduction reactions · porous carbon

Figure 9. (A) LSV curves of BNC-5 composite before (black) and after (red) 5000 CV cycles. Inset shows the CV curves of BNC-5 composite before (black) and after (red) 5000 CV cycles. (B) LSV curves of BNC-5 composite in the presence (red) and absence of (black) methanol. Inset shows the CV curves of BNC-5 composite in the presence (red) and absence of (black) methanol. The methanol concentration is 3 M.

[1] B. M. Sanchez, Y. Gogotsi, *Adv. Mater.* **2016**, *28*, 6104–6135.
[2] M. M. Liu, R. Z. Zhang, W. Chen, *Chem. Rev.* **2014**, *114*, 5117–5160.
[3] J. Yu, C. L. Wang, W. J. Yuan, Y. H. Shen, A. J. Xie, *Chem. Eur. J.* **2019**, *25*, 2877–2883.
[4] M. R. Liu, Q. L. Hong, Q. H. Li, Y. Du, H. X. Zhang, S. Chen, T. Zhou, J. Zhang, *Adv. Funct. Mater.* **2018**, *28*, 1801136.
[5] C. F. Dickens, I. Chorkendorff, J. K. Norskov, T. F. Jaramillo, *Science* **2017**, *355*, eaad4998.
[6] X. W. Zhou, X. Liu, J. H. Zhang, C. Zhang, S. J. Yoo, J. G. Kim X Y Chu, C. Song, P. Wang, Z. Z. Zhao, D. B. Li, W. Zhang, W. T. Zheng, *Carbon* **2020**, *166*, 284–290.
[7] L. Yang, J. Shui, L. Du, Y. Shao, J. Liu, L. Dai, Z. Hu, *Adv. Mater.* **2019**, *31*, 1804799.
[8] X. Sun, D. Li, Y. Ding, W. Zhu, S. Guo, Z. L. Wang, S. Sun, *J. Am. Chem. Soc.* **2014**, *136*, 5745–5749.
[9] Z. Lu, J. Wang, S. Huang, Y. Hou, Y. Li, Y. Zhao, S. Mu, J. Zhang, Y. Zhao, *Nano Energy* **2017**, *42*, 334–340.
[10] J. C. Li, P. X. Hou, M. Cheng, C. Liu, H. M. Cheng, M. H. Shao, *Carbon* **2018**, *139*, 156–163.
[11] R. G. Ma, G. X. Lin, Y. Zhou, Q. Liu, T. Zhang, G. C. Shan, M. H. Yang, J. C. Wang, *NPJ Computational Mater.* **2019**, *5*, 78.
[12] D. H. Guo, R. Shibuya, C. Akiba, S. Saji, T. Kondo, J. Nakamura, *Science* **2016**, *351*, 361–365.

[13] P. Y. Bai, W. Q. Liu, C. C. Yang, S. L. Wei, L. Xu, *J. Colloid Interface Sci.* **2021**, *587*, 290–301.

[14] Y. Y. She, J. F. Chen, C. X. Zhang, Z. G. Lu, M. Ni, P. H. L. Sit, M. K. H. Leung, *Appl. Energy* **2018**, *225*, 513–521.

[15] M. X. Zhang, D. Wu, Y. X. Ye, L. Wu, Z. Z. Yao, X. L. Ma, L. H. Wang, Z. J. Zhang, S. C. Xiang, *ChemPlusChem* **2018**, *83*, 1044–1051.

[16] J. Y. Zhang, G. Zhang, S. Y. Jin, Y. J. Zhou, Q. H. Ji, H. C. Lan, H. J. Liu, J. H. Qu, *Carbon* **2020**, *163*, 154–161.

[17] X. Wang, Y. Liu, P. Wu, *Chem. Eng. J.* **2017**, *328*, 417–427.

[18] C. Zhu, M. Takata, Y. Aoki, H. Habazaki, *Chem. Eng. J.* **2018**, *350*, 278–289.

[19] C. H. Choi, M. W. Chung, H. C. Kwon, S. H. Park, S. I. Woo, *J. Mater. Chem. A* **2013**, *1*, 3694–3699.

[20] Y. Y. Guo, P. F. Yuan, J. N. Zhang, Y. F. Hu, I. S. Amiinu, X. Wang, J. G. Zhou, H. C. Xia, Z. B. Song, Q. Xu, S. C. Mu, *ACS Nano* **2018**, *12*, 1894–1901.

[21] Z. K. Kou, B. B. Guo, D. P. He, J. Zhang, S. C. Mu, *ACS Energy Lett.* **2018**, *3*, 184–190.

[22] J. M. Wang, J. Hao, D. Liu, S. Qin, C. Chen, C. Yang, Y. C. Liu, T. Y. Yang, Y. Fan, Y. Chen, W. W. Lei, *Nanoscale* **2017**, *9*, 9787–9791.

[23] F. Zhang, C. Zhao, S. Chen, H. Li, H. Yang, X. M. Zhang, *J. Catal.* **2017**, *348*, 212–222.

[24] Y. J. Lee, H. J. Joo, L. R. Radovic, *Carbon* **2003**, *41*, 2591–2600.

[25] X. X. Wu, L. R. Radovic, *Carbon* **2005**, *43*, 1768–1777.

[26] S. L. Ding, S. J. Zheng, M. J. Xie, L. M. Peng, X. F. Guo, W. P. Ding, *Microporous Mesoporous Mater.* **2011**, *142*, 609–613.

[27] C. J. Zhao, Y. W. Ding, Y. X. Huang, N. Li, Y. Q. Hu, C. H. Zhao, *Appl. Surf. Sci.* **2021**, *555*, 149726.

[28] Y. C. Wang, Y. S. Liu, H. F. Yang, Y. Liu, K. H. Wu, G. C. Yang, *J. Colloid Interface Sci.* **2020**, *579*, 637–644.

[29] W. Wang, Q. Jia, S. Mukerjee, S. Chen, *ACS Catal.* **2019**, *9*, 10126–10141.

[30] D. Hulicova-Jurcakova, M. Seredych, G. Q. Lu, T. J. Bandosz, *Adv. Funct. Mater.* **2009**, *19*, 438–447.

[31] T. Sun, J. Wang, C. Qiu, X. Ling, B. Tian, W. Chen, C. Su, *Adv. Sci.* **2018**, *5*, 1800036.

[32] E. Iyyamperumal, S. Wang, L. Dai, *ACS Nano* **2012**, *6*, 5259–5265.

[33] Y. Xu, J. Y. Cheng, P. M. Yiu, G. C. Shan, T. Shibayama, S. Watanabe, M. Ohnuma, C.-H. Shek, *Nanoscale* 18846–18856.

[34] M. Xiao, J. Zhu, L. Feng, C. Liu, W. Xing, *Adv. Mater.* **2015**, *27*, 2521–2527.

[35] W. Wei, H. Liang, K. Parvez, X. Zhuang, X. Feng, K. Mullen, *Angew. Chem. Int. Ed.* **2014**, *53*, 1570–1574; *Angew. Chem.* **2014**, *126*, 1596–1600.

[36] H. W. Liang, X. Zhuang, S. Bruller, X. Feng, K. Mullen, *Nat. Commun.* **2014**, *5*, 4973–4980.

[37] C. Q. Jesica, B. G. Esther, J. P. F. Francisco, C. M. Francisco, F. P. C. Agustín, *Carbon* **2019**, *155*, 88–99.

[38] X. G. Li, L. Ni, J. H. Zhou, L. Xu, C. L. Lu, G. X. Yang, W. P. Ding, W. H. Hou, *Nanoscale* **2020**, *12*, 13987–13995.

[39] L. Xiao, J. M. Yang, G. Y. Huang, Y. Zhao, H. B. Zhu, *Inorg. Chem. Commun.* **2020**, *118*, 107982.

[40] S. S. Zhang, X. Y. Liu, Z. H. Li, L. Hao, P. H. Wang, X. R. Zou, Z. J. Liu, G. J. Zhang, C.-Y. Zhang, *ACS Sustainable Chem. Eng.* **2019**, *7*, 11787–11794.

[41] X. L. Xing, R. J. Liu, M. Anjass, K. C. Cao, U. Kaiser, G. J. Zhang, C. Streb, *Appl. Catal. B* **2020**, *277*, 119195.

[42] F. X. Wang, Y. M. Liu, C.-Y. Zhang, *New J. Chem.* **2019**, *43*, 4160–4167.

[43] B. Konkena, K. J. Puring, I. Sinev, S. Piontek, O. Khavryuchenko, J. P. Dürholt, R. Schmid, H. Tüysüz, M. Muhler, W. Schuhmann, U. P. Apfel, *Nat. Commun.* **2016**, *7*, 12269.